JDSI JOURNAL OF DEFENCE AND SECURITY INDUSTRY

Journal of Defence and Security Industries: Strategy and Technology, 2026; 1(2)

Science & Technology Section

Mechanically Alloyed Nd-Fe-B Nanoparticles with Graphitic Carbon Shell: Synthesis, Characterization and Magnetic Properties

Mustafa Bellek[1,*], Sina Kavak [1], Duygu Ağaoğulları[2]

Abstract

In this study, Nd-Fe-B nanoparticles with permanent magnet properties were synthesized from elemental raw materials using the mechanical alloying (MA) method and subsequently encapsulated with graphitic carbon shell to enhance their thermal and chemical stability for potential electronic applications. Alloy composition Nd ≈ 23.3 wt.%, Fe ≈ 75.7 wt.%, B ≈ 1.0 wt.%, $Nd_{10}Fe_{84}B_6$ atomic composition, were milled for varying durations 8-10 and 12 h to evaluate the effects of milling duration on magnetic performance. Due to high-energy milling, powder yield remained between 41% and 53%, influenced by particle adhesion and partial melting. X-ray Diffraction (XRD) confirmed the formation of the tetragonal $Nd_2Fe_{14}B$ phase in all MA-synthesized powders, while Dynamic Light Scattering (DLS) and Scanning Electron Microscopy (SEM) analyses verified nanoparticle size and agglomerated morphologies characteristic of welding-fracture-rewelding cycles in MA. Annealing at 900°C for 1 h improved crystallinity and promoted the formation of additional phases, as supported by XRD, SEM and Energy Dispersive Spectroscopy (EDS) results. A Graphitic Carbon Shell (GCS) was successfully deposited on the nanoparticle surfaces via Chemical Vapor Deposition (CVD) under a CH_4/H_2 atmosphere at 950°C; the presence of the carbonaceous coating was confirmed by XRD and elemental mapping. Transmission Electron Microscopy (TEM) analysis revealed the core-shell structure, the number of graphitic carbon shell layers, and the uniformity of the encapsulation surrounding the nanoparticles. Magnetic characterization using Vibrating Sample Magnetometer (VSM) showed variations in coercivity, saturation magnetization and remanence before and after encapsulation. Among all samples, the 10 h milled, annealed and graphitic carbon shell encapsulated sample (NFB2TG) exhibited the most favorable magnetic properties, reaching a coercivity of 185.71 Oe and saturation magnetization of 46.3 emu/g. These results demonstrate that MA followed by annealing and encapsulation GCS is a promising route for producing stable Nd-Fe-B nanoparticles.

Keywords: Nd-Fe-B nanoparticles, mechanical alloying, graphitic carbon shell encapsulation, chemical vapor deposition, magnetic properties.

Received: 25.11.2025 Accepted: 22.05.2026 Research Article

[1]ASELSAN Inc., Ankara, Türkiye
[2] Istanbul Technical University, Istanbul, Türkiye
* Corresponding author.
✉ mubellek@aselsan.com

Cite this article as:
https://doi.org/10.65834/jdsi.12.46
Bellek, M., Kavak, S. & Ağaoğulları, D. (2026). Mechanically Alloyed Nd-Fe-B Nanoparticles with Graphitic Carbon Shell: Synthesis, Characterization and Magnetic Properties. *Journal of Defence and Security Industries: Science & Technology Section 2(1)*, 177-200.

1. Introduction

The main goal in studies on magnetism has been to develop more powerful permanent magnets. Rare Earth (RE)-Fe-B permanent magnets are known for their superior magnetic properties, in which Neodymium (Nd) is generally used as the RE element. They are frequently preferred in industry due to their lower cost compared to Sm-Co magnets (Wu et al., 1997). Various production methods exist for Nd-Fe-B permanent magnets: Powder Metallurgy (PM), melt spinning, hot deformation and Hydrogen Decrepitation Desorption Recombination (HDDR) (Rahimi et al., 2017; Zhou et al., 2019). The primary objective of these methods is to produce anisotropic Nd-Fe-B magnets with improved magnetic properties. Chemical synthesis of $Nd_2Fe_{14}B$ nanoparticles with tetragonal lattice structure is challenging due to the high reduction potential of Nd^{3+} and the oxidation tendency of $Nd_2Fe_{14}B$ (Rahimi et al., 2017).

It is anticipated that Nd-Fe-B nanoparticles produced by solid-state synthesis methods will exhibit favorable saturation magnetization and coercivity values (De Moraes et al., 2024; Schultz et al., 1987). However, their high surface area makes them chemically reactive, necessitating surface coating (Jung et al., 2024). Several methods have been investigated to increase the oxidation resistance of Nd-Fe-B magnets (Lee et al., 2005; Liu et al., 2012; Pich et al., 2005). While alloying can also enhance oxidation resistance, it frequently degrades magnetic properties, making protective coatings the preferred approach for practical applications (Chen et al., 2007; Tung et al., 2015).

In the literature, Nd-Fe-B magnetic materials have been synthesized in a variety of forms through distinct production routes. Nanoparticles synthesized from a Nd-Fe-B alloy using hydrogen decrepitation and high-energy ball milling have been investigated for their efficacy as Magnetic Hyperthermia (MH) agents. Périgo et al. (2012) found that the resulting materials, characterized by a mixed-phase structure, demonstrated superior heating capabilities. Under an applied Alternating Current (AC) magnetic field (3.7 kA m^{-1}, 228 kHz), a maximum estimated Specific Absorption Rate (SAR) of approximately 2500 W kg^{-1} was recorded. The study also confirmed acceptable in vitro biocompatibility attributed to a protective coating applied during milling. The development of high-performance magnetic nanoparticles necessitates continuous optimization of synthesis techniques, particularly ball milling methods, to control both size and shape. Chakka et al. (2006) utilized surfactant-assisted ball milling in an organic carrier liquid to synthesize Nd-Fe-B nanoparticles with a narrow size distribution below 30 nm. Their investigation highlighted a key morphological distinction: while Fe and Fe-Co particles were largely spherical, Nd-Fe-B, Co and Sm-Co nanoparticles exhibited elongated rod shapes, with most systems displaying superparamagnetic behavior at room temperature. Zhang et al. (2018) successfully employed a sol-gel process, using citric acid and glycol, to prepare Nd-Fe-B nanoparticles consistently below 100 nm. Their method relied on a two-step thermal treatment: an initial annealing to form oxide precursors and a subsequent reductive annealing to yield the final metallic Nd-Fe-B nanoparticles. As confirmed by Vibrating Sample Magnetometer (VSM) analysis, the saturation magnetization increased substantially from 1.08 emu/g to 14.17

emu/g, validating successful hard magnetic phase formation. Mehrifar et al. (2025) demonstrated the synthesis of $Nd_2Fe_{14}B$ nanoparticles using ethanol-assisted wet ball milling, efficiently reducing the starting powder size through prolonged milling.

In addition to synthesis investigations, coating studies have been conducted to enhance oxidation resistance, chemical and thermal stability. Hosseinabadi et al. (2019) reported that Nd-Fe-B powders developed a thin amorphous carbon layer derived from oleic acid surfactant during high-energy wet ball milling. Increasing the surfactant concentration produced a thicker carbonaceous coating, enhancing the imaginary part of dielectric permittivity by approximately 95%, increasing absorption shielding efficiency by about 40% and total shielding efficiency by nearly 30% at certain frequencies, attributed to improved impedance matching and strengthened microwave absorption. Ouyang et al. (2019) demonstrated that a polydopamine-based magnetic fluid coating provided exceptional corrosion inhibition, with corrosion current density of 1.74×10^{-3} mA/cm² in 3.5 wt.% NaCl solution over 30 days, roughly three orders of magnitude lower than bare Nd-Fe-B (1.01 mA/cm²), and excellent self-healing behavior after mechanical damage. Shen et al. (2018) improved corrosion resistance of sintered Nd-Fe-B magnets using Ni-Al_2O_3 nanocomposite coatings via pulsed current-jet electrodeposition, finding that nanoparticle incorporation enhanced both adhesion strength and corrosion resistance over pure nickel coatings. Yang et al. (2022) modified multiwall Carbon Nanotubes (CNTs) via noncovalent functionalization with tannic acid to form Tannic Acid Functionalized Carbon Nanotubes (TCNTs) hybrids and incorporated them into epoxy coatings on sintered Nd-Fe-B magnets. Electrochemical tests showed specimens with 2 g/L TCNTs maintained a high impedance ($|Z|_{0.01Hz} \approx 10^8\ \Omega\ cm^2$) after 36 days in 3.5 wt.% NaCl solution, demonstrating excellent corrosion resistance. Bystrzejewski et al. (2007) produced carbon nanoencapsulates of 20-50 nm using an arc discharge method with graphite anodes doped with $Nd_2Fe_{14}B$, achieving a maximum coercive force of approximately 413 Oe.

Nd-Fe-B nanoparticles have a wide range of potential applications. In biomedicine, they are used for targeted drug delivery, MH and Magnetic Resonance Imaging (MRI) enhancement (Iacovacci et al., 2015; Omelyanchik et al., 2020; Saritas et al., 2012). They have also been investigated for Micro-Electro-Mechanical Systems (MEMS) devices (Dempsey, 2009; Lecerf et al., 2025) and magnetically recoverable catalysts (Yang et al., 2019). Their main limitation is rapid oxidation, necessitating protective encapsulation with carbon, silica or polymer shells.

In this study, Nd-Fe-B nanoparticles were synthesized via Mechanical Alloying (MA), a process driven by cyclical cold welding, fracturing and re-welding of elemental powders to achieve a refined, homogeneous microstructure (Ağaoğulları et al., 2011; Ağaoğulları et al., 2017; Suryanarayana, 2010). The $Nd_{10}Fe_{84}B_6$ composition was selected because it is slightly Fe-rich relative to the stoichiometric $Nd_2Fe_{14}B$ phase ($Nd_{11.76}Fe_{82.35}B_{5.88}$ at. %). This Fe-rich, Nd-lean composition promotes the simultaneous formation of hard magnetic $Nd_2Fe_{14}B$ and soft magnetic α-Fe phases during MA and annealing. The exchange coupling between these two nanoscale phases is known to enhance remanence beyond the single-phase limit, and this composition has been widely investigated in nanocrystalline Nd-Fe-B systems (Manaf et al.,

1993; Schultz et al., 1987). Nanoparticles were milled for 8, 10 and 12 h, followed by annealing at 900°C. Comprehensive characterization using X-Ray Diffraction (XRD), Dynamic Light Scattering (DLS), Scanning Electron Microscopy (SEM) and Energy Dispersive Spectroscopy (EDS) confirmed the successful synthesis of nanoscale particles containing the $Nd_2Fe_{14}B$ tetragonal phase. Following annealing, the powders were subjected to Chemical Vapor Deposition (CVD) at 950°C for Graphitic Carbon Shell (GCS) encapsulation. Transmission Electron Microscopy (TEM) analysis revealed a distinct core-shell architecture with a continuous GCS surrounding the nanoparticles. The optimized sample (NFB2TG) exhibited a coercivity of 185.71 Oe and a saturation magnetization of 46.3 emu/g, demonstrating that GCS-encapsulated, MA-synthesized Nd-Fe-B nanoparticles represent a promising route for producing chemically stable magnetic nanoparticles.

2. Methodology

2.1. Powder Preparation

Neodymium powders (Nanografi A.Ş., 99.5% purity, ~325 μm) were combined with Fe powders (Alfa Aesar, ~44 μm) and B powders (Pavezyum Kimya, <1 μm). Powder mixtures of 3 g each were prepared in the $Nd_{10}Fe_{84}B_6$ composition, corresponding to Nd ≈ 23.3 wt.%, Fe ≈ 75.7 wt.% and B ≈ 1.0 wt.%, giving 0.70 g Nd, 2.27 g Fe and 0.03 g B per batch. All powder handling was performed in a glove box (MBraun™ LABstar) under a high-purity Ar atmosphere (Linde™, 99.999%), with O_2 and H_2O levels below 5 ppm. The powders were transferred into stainless steel vials sealed under Ar and prepared for milling at a powder-to-ball ratio of 1:10 using 6 mm diameter stainless steel balls.

2.2. Mechanical Alloying

Powder mixtures were milled for 8, 10 and 12 h in a high-energy ball mill (Spex™ 8000D Mixer/Mill). After milling, the vials were cooled at room temperature for approximately 12 h in air, then opened inside the glove box under Ar to prevent oxidation. Samples milled for 8, 10 and 12 h were designated NFB1, NFB2 and NFB3, respectively. After annealing, the letter ‘T’ was appended as NFB1T, NFB2T, NFB3T; after graphitic carbon shell encapsulation, ‘G’ was further appended, yielding NFB1TG, NFB2TG and NFB3TG. Sample designations are summarized in Table 1.

Table 1. Sample designations as a function of milling duration and applied processing steps.

Sample Name	Milling Time (h)	MA	Annealed	Graphitic Carbon Shell Encapsulated
NFB1	8	Yes	No	No
NFB2	10	Yes	No	No
NFB3	12	Yes	No	No
NFB1T	8	Yes	Yes	No
NFB2T	10	Yes	Yes	No
NFB3T	12	Yes	Yes	No
NFB1TG	8	Yes	Yes	Yes
NFB2TG	10	Yes	Yes	Yes
NFB3TG	12	Yes	Yes	Yes

2.3. Annealing Process

Following mechanical alloying, the $Nd_{10}Fe_{84}B_6$ powders containing the tetragonal $Nd_2Fe_{14}B$ phase were annealed to increase the proportion of this phase and improve crystallinity. Annealing was performed in a temperature- and pressure-controlled tube furnace (PROTHERM™ Furnaces), as shown in Figure 1, under flowing Ar (100 ml/min) at 50 mbar.

The annealing procedure (Figure 2) consisted of three sequential stages: (1) heating from room temperature to 900°C over 1 h, (2) isothermal holding at 900°C for 1 h, and (3) controlled cooling from 900°C to 300°C over 1 h. Ar flow and vacuum were maintained until room temperature was reached, after which the system was switched off and allowed to cool naturally.

Figure 1. Annealing experimental setup (PROTHERM™ Furnaces).

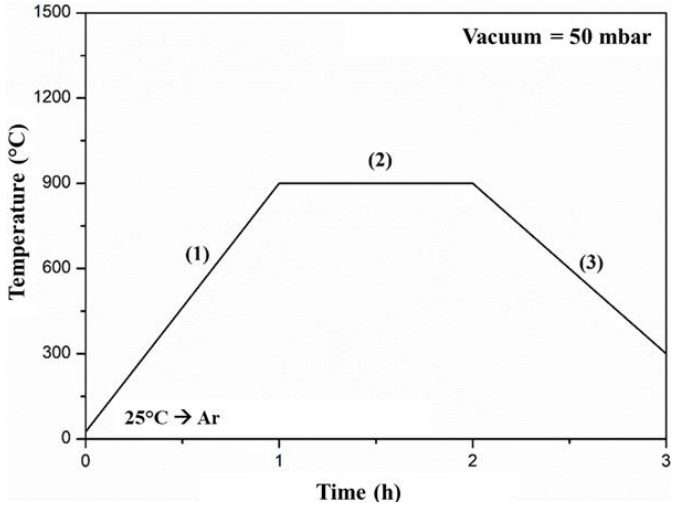

Figure 2. Annealing process regime.

2.4. Graphitic Carbon Shell Encapsulation

Following annealing, all samples were subjected to CVD encapsulation in a temperature-controlled tube furnace (PROTHERM™ Furnaces) under 50 mbar vacuum, using H_2 (Linde™, 99.99%) and CH_4 (Linde™, 99.99%) as carrier and carbon precursor gases, respectively.

The CVD procedure (Figure 3) comprised three stages: (1) Heating from room temperature to 950°C over 1 h, (2) Isothermal holding at 950°C for 1 h to promote carbon deposition, and (3) Controlled cooling from 950°C to 300°C over 1 h. H_2 was introduced at room temperature at 100 ml/min; CH_4 was introduced at 550°C at the same flow rate. Both gases were shut off at 550°C during cooling while the vacuum was maintained until room temperature was reached. The resulting coating is referred to throughout as a graphitic carbon shell, as confirmed by XRD and TEM.

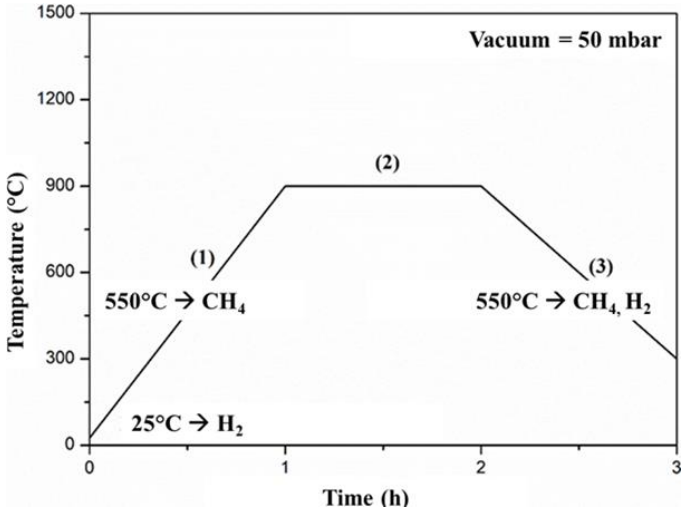

Figure 3. Chemical Vapor Deposition (CVD) process parameter regime.

3. Results

The Nd-Fe-B powder mixtures were prepared in the $Nd_{10}Fe_{84}B_6$ atomic composition, corresponding to 0.70 g Nd, 2.27 g Fe and 0.03 g B per 3 g batch. Figure 4 presents the XRD patterns following mechanical alloying for 8, 10 and 12 h. The $Nd_2Fe_{14}B$ phase with tetragonal crystal structure was confirmed in all three samples. Alongside the primary $Nd_2Fe_{14}B$ phase, α-Fe and Fe_2O_3 phases were identified. The presence of Fe_2O_3 indicates partial surface oxidation during the air-cooling period following milling. Given the high surface area and chemical reactivity of $Nd_2Fe_{14}B$ nanoparticles, even brief air exposure is sufficient to promote oxidation, which is expected to influence the magnetic properties and phase distribution.

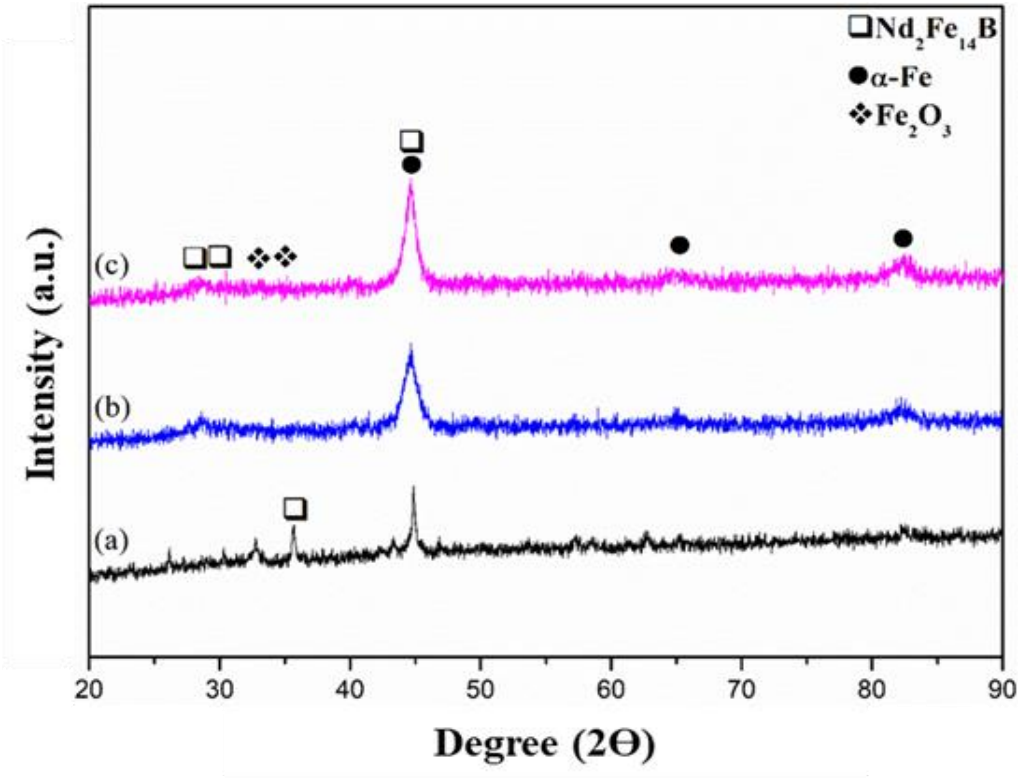

Figure 4. X-Ray Diffraction (XRD) pattern of the samples; **(a)** NFB1, **(b)** NFB2, **(c)** NFB3.

DLS analysis of the NFB1, NFB2 and NFB3 samples yielded average hydrodynamic sizes of 15.48 nm, 20.83 nm and 146.3 nm for the 8, 10 and 12 h milled samples, respectively. It should be noted that DLS measures the hydrodynamic diameter of agglomerates in suspension rather than true primary particle size. As reported by Lim et al. (2013), DLS is highly sensitive to agglomeration in magnetic nanoparticle systems and can significantly overestimate primary particle dimensions due to agglomerate contributions to the light scattering signal. Furthermore, Jia et al. (2023) noted that scattering intensity scales with the sixth power of particle diameter, meaning agglomerates dominate the signal and mask the true primary particle size. The apparent increase in measured size with longer milling durations is therefore attributed to progressive agglomeration rather than grain growth, consistent with findings by

Mehrifar et al. (2025) for dry ball-milled $Nd_2Fe_{14}B$ systems. A TEM-based primary particle size analysis would be required to accurately determine individual particle dimensions, and this is acknowledged as a limitation of the current characterization approach.

Figure 5 presents SEM images of NFB1, NFB2 and NFB3 at 500×, 1000× and 3000× magnifications. Pronounced agglomeration is evident in all samples, forming irregularly shaped clusters. This is characteristic of the MA process, in which repeated cold welding, fracturing and re-welding promote strong interparticle bonding (Ağaoğulları et al., 2011; Suryanarayana, 2010). Strong magnetic dipole-dipole interactions inherent to Nd-Fe-B systems further drive agglomeration upon air exposure. SEM reveals agglomerate morphology rather than individual primary particles; agglomerate sizes are consistent with the DLS measurements. The degree of agglomeration increases with milling duration, with NFB3 displaying larger and more densely packed structures, consistent with progressive oxidation-enhanced surface reactivity at longer milling times.

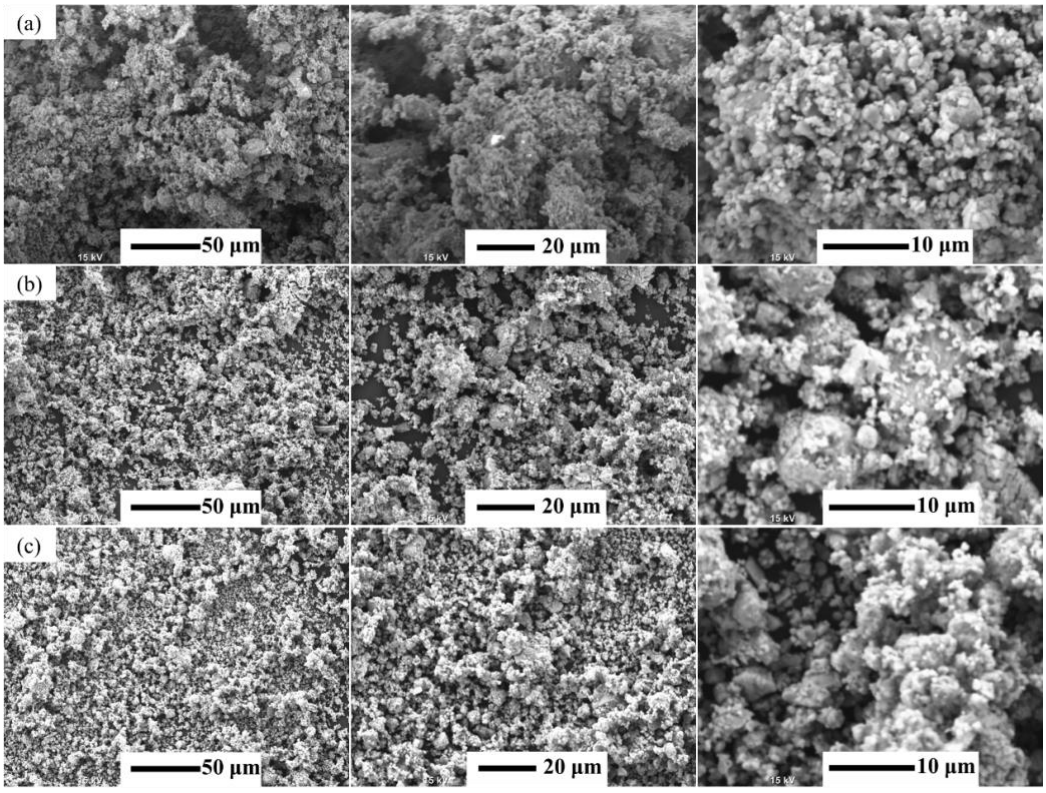

Figure 5. Scanning Electron Microscopy (SEM) images at 500X, 1000X and 3000X magnifications: **(a)** NFB1, **(b)** NFB2 and **(c)** NFB3.

Figure 6 shows the EDS analysis points on SEM images of NFB1, NFB2 and NFB3, with elemental results in Table 2. NFB1 and NFB3 show close agreement between two analysis points, indicating relatively homogeneous elemental distributions. NFB2 shows lower Fe content and greater variability between points. EDS is inherently unreliable for quantitative boron detection due to the low atomic number of boron (Z = 5), resulting in characteristic X-

rays of insufficient energy for accurate quantification (Goldstein et al., 2018). The boron values reported in Table 2, including elevated B concentrations in NFB2, should be treated as semi-quantitative estimates only. The target composition was Nd ≈ 23.3 wt.%, Fe ≈ 75.7 wt.%, B ≈ 1.0 wt.%; among the three samples, NFB1 shows the closest agreement with this intended distribution.

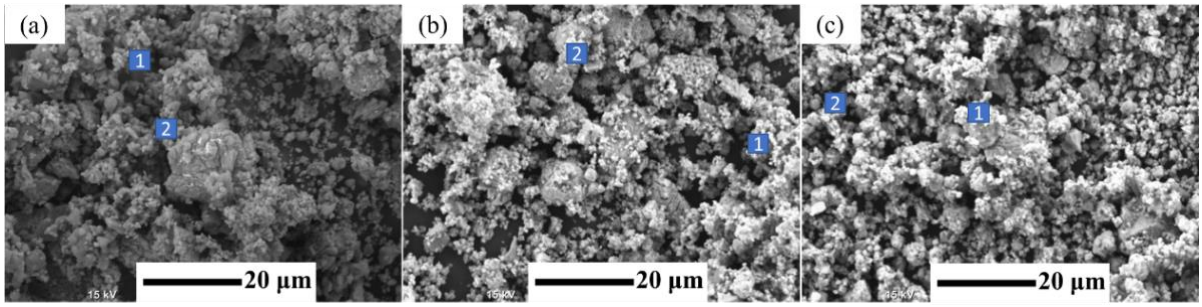

Figure 6. Energy Dispersive Spectroscopy (EDS) analysis points marked on the SEM images of the mechanically alloyed powders: **(a)** NFB1, **(b)** NFB2 and **(c)** NFB3.

Table 2. Energy Dispersive Spectroscopy (EDS) analysis results correspond to the points shown in Figure 6.

Sample	**Elemental Ratio**		
NFB1	**Nd%**	**Fe%**	**B%**
1	25.83	74.17	0
2	26.64	74.36	0
NFB2	**Nd%**	**Fe%**	**B%**
1	25.10	69.44	5.46
2	21.71	57.55	20.74
NFB3	**Nd%**	**Fe%**	**B%**
1	25.92	74.08	0
2	27.08	72.92	0

Figure 7 presents the VSM hysteresis curve of NFB2. The sample exhibits a coercivity of 54.81 Oe, a saturation magnetization of 133.43 emu/g and a remanent magnetization of 2.83 emu/g under approximately 2 T. While the saturation magnetization falls within the expected range for Nd-Fe-B systems, the coercivity of 54.81 Oe is notably below values reported for bulk sintered Nd-Fe-B magnets, typically exceeding 10,000 Oe (Coey, 2010). The as-milled sample behaves as a magnetically soft material, reflecting: (1) the heavily strained, partially amorphous microstructure limiting $Nd_2Fe_{14}B$ crystallization and magnetocrystalline anisotropy development; (2) soft magnetic α-Fe and non-magnetic Fe_2O_3 secondary phases reducing effective anisotropy; and (3) disordered surface spins at the high-surface-area nanoparticle

boundaries suppressing coercivity. The low remanence ratio (Mr/Ms ≈ 0.021) confirms an isotropic, exchange-decoupled system.

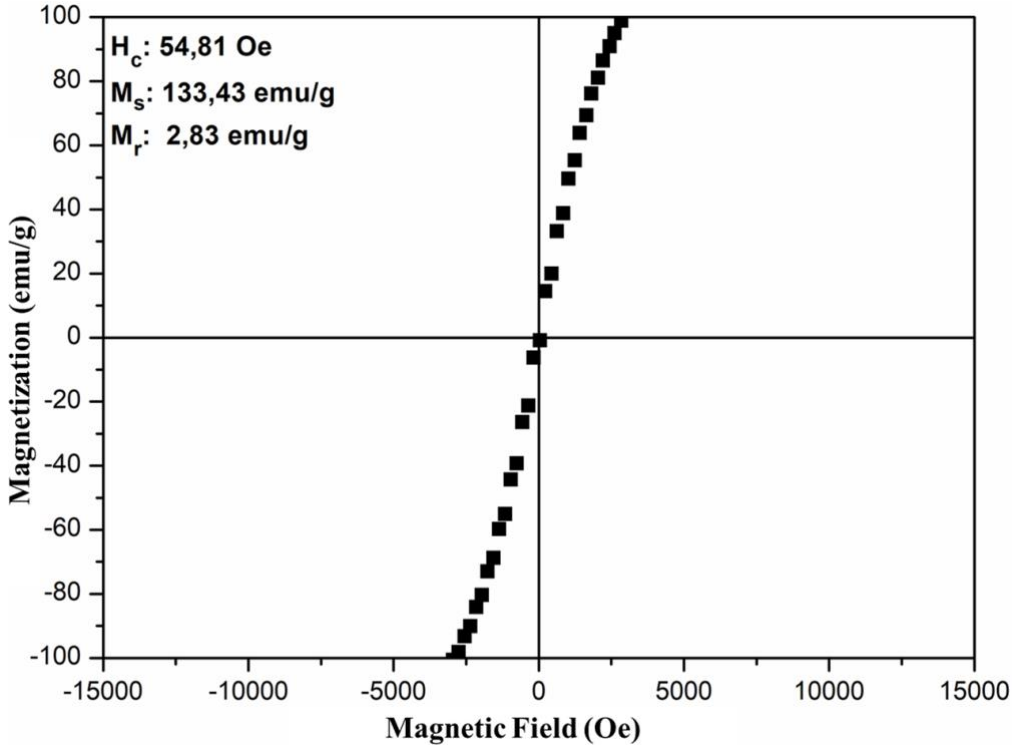

Figure 7. Vibrating sample magnetometer (VSM) analysis result shown on the hysteresis curve of the NFB2 sample.

Figure 8 presents XRD patterns of NFB1T, NFB2T and NFB3T following annealing at 900°C for 1 h. The $Nd_2Fe_{14}B$ tetragonal phase is confirmed in all three samples, with notably increased peak intensities compared to as-milled counterparts (Figure 4), indicating significant improvement in crystallinity. The sharpening of $Nd_2Fe_{14}B$ diffraction peaks is consistent with grain growth and the transformation of the partially amorphous as-milled structure into a more ordered crystalline state. The α-Fe and Fe_2O_3 phases remain present. Persistence of Fe_2O_3 confirms that oxidation is not eliminated by thermal treatment under Ar, suggesting surface oxidation had progressed significantly prior to annealing. The continued α-Fe is expected for the Fe-rich $Nd_{10}Fe_{84}B_6$ composition, as excess iron segregates as a soft magnetic phase. While the resulting $Nd_2Fe_{14}B$/α-Fe nanocomposite can theoretically enhance remanence through exchange coupling, the simultaneous presence of non-magnetic Fe_2O_3 dilutes the effective magnetic moment and limits coercivity development.

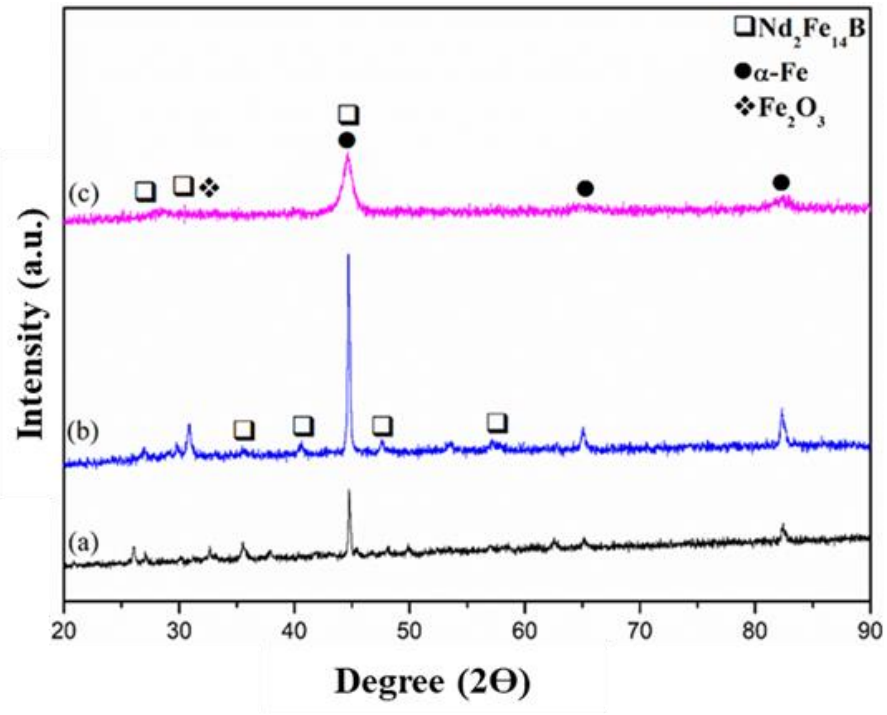

Figure 8. XRD patterns of the annealed samples produced in the Nd-Fe-B composition: **(a)** NFB1T, **(b)** NFB2T, **(c)** NFB3T.

Figure 9 presents SEM images of NFB1T, NFB2T and NFB3T. Agglomeration persists after annealing, consistent with as-milled morphology (Figure 5). However, the annealed samples display a more defined spherical particle shape, attributed to surface energy minimization during annealing, whereby atomic diffusion and rearrangement drive the formation of more energetically favorable spherical geometries. The degree of agglomeration is comparable across the three conditions, suggesting that 900°C annealing did not promote significant interparticle sintering. The pre-existing oxidized surface layer is expected to act as a diffusion barrier limiting grain boundary migration.

Figure 10 shows EDS analysis points for NFB1T, NFB2T and NFB3T, with results in Table 3. In NFB1T and NFB2T, an increase in Nd content accompanied by a decrease in Fe content is observed relative to the as-milled state. This compositional shift is consistent with Nd redistribution during annealing, whereby Nd-rich phases segregate toward grain boundaries and particle surfaces at elevated temperatures, a phenomenon well documented in Nd-Fe-B systems (Sepehri-Amin et al., 2014). NFB3T shows the opposite trend, suggesting a different local phase distribution resulting from more extensive structural changes during 12 h milling. Among the annealed samples, NFB2T shows the closest agreement with the $Nd_{10}Fe_{84}B_6$ target composition. As previously established, EDS boron values should be treated as semi-quantitative only (Goldstein et al., 2018).

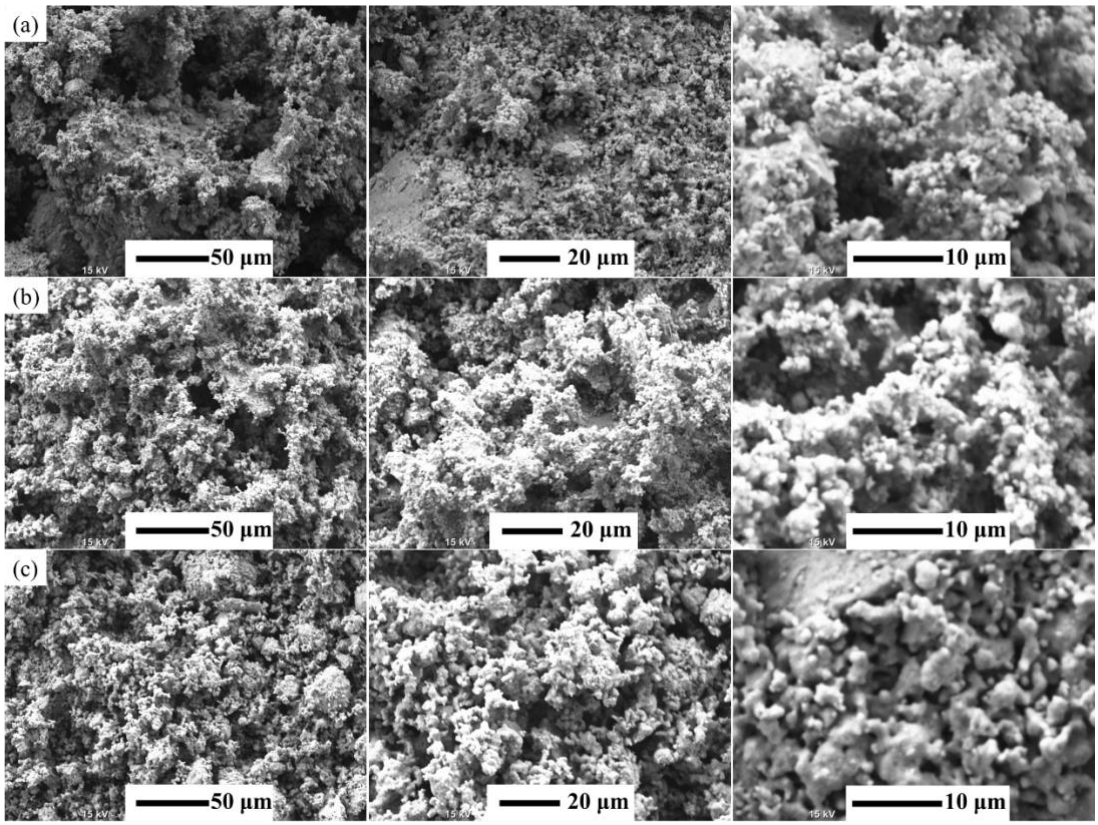

Figure 9. SEM images of the annealed Nd-Fe-B samples at 500X, 1000X and 3000X magnifications: **(a)** NFB1T, **(b)** NFB2T, **(c)** NFB3T.

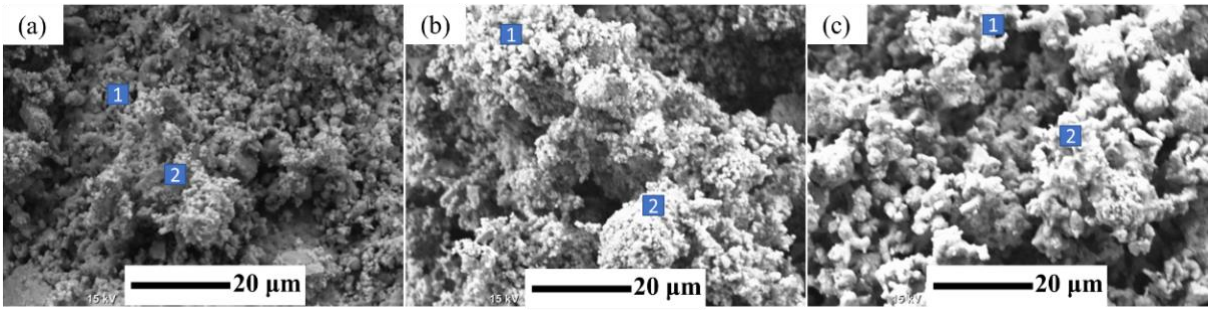

Figure 10. EDS analysis points marked on the SEM images of the mechanically alloyed and annealed Nd-Fe-B powders: **(a)** NFB1T, **(b)** NFB2T, **(c)** NFB3T.

Table 3. EDS results correspond to the points shown in Figure 10.

Sample	**Elemental Ratio**		
NFB1T	**Nd%**	**Fe%**	**B%**
1	30.08	69.92	0
2	27.93	72.07	0
NFB2T	**Nd%**	**Fe%**	**B%**
1	26.86	73.14	0
2	27.67	72.33	0
NFB3T	**Nd%**	**Fe%**	**B%**
1	24.95	75.05	0
2	18.94	73.23	7.83

Figure 11 presents VSM hysteresis curves of NFB1T, NFB2T and NFB3T under a 2 T field. Annealing produced a clear coercivity improvement across all samples. For NFB2T, coercivity increased from 54.81 Oe to 107.77 Oe, an approximate doubling, attributed to crystallinity restoration and recovery of magnetocrystalline anisotropy in the $Nd_2Fe_{14}B$ phase (Popa et al., 2013). Conversely, saturation magnetization decreased slightly from 133.43 to 128.90 emu/g, likely due to continued growth of non-magnetic Fe_2O_3 during annealing, which dilutes the net magnetic moment. This coercivity-Ms trade-off is a recognized behavior in mechanically alloyed Nd-Fe-B systems (Savchenko et al., 2018). NFB2T exhibits the highest coercivity among the annealed samples, while NFB3T records the highest Ms, consistent with a greater α-Fe proportion from 12 h milling. All annealed samples remain in the semi-hard magnetic regime, well below bulk sintered Nd-Fe-B values (>10,000 Oe), due to residual oxidation, secondary phase presence and isotropic grain orientation.

Figure 12 presents XRD patterns of NFB1TG, NFB2TG and NFB3TG following CVD encapsulation. A distinct carbon peak is observed at $2\theta \approx 27°$ in all three samples, corresponding to the (002) reflection of graphitic carbon, confirming successful carbonaceous layer deposition. The interlayer spacing associated with this peak is consistent with ordered graphitic stacking, suggesting a graphitic carbon shell rather than amorphous carbon. However, XRD alone is insufficient to conclusively determine graphene layer number or coating quality; Raman spectroscopy would be required for definitive assessment, an acknowledged limitation. The $Nd_2Fe_{14}B$ tetragonal phase and α-Fe peaks are retained, confirming that CVD at 950°C did not degrade the hard magnetic phase. Fe_2O_3 peaks persist, indicating the pre-existing oxide layer was not reduced under the CH_4/H_2 atmosphere.

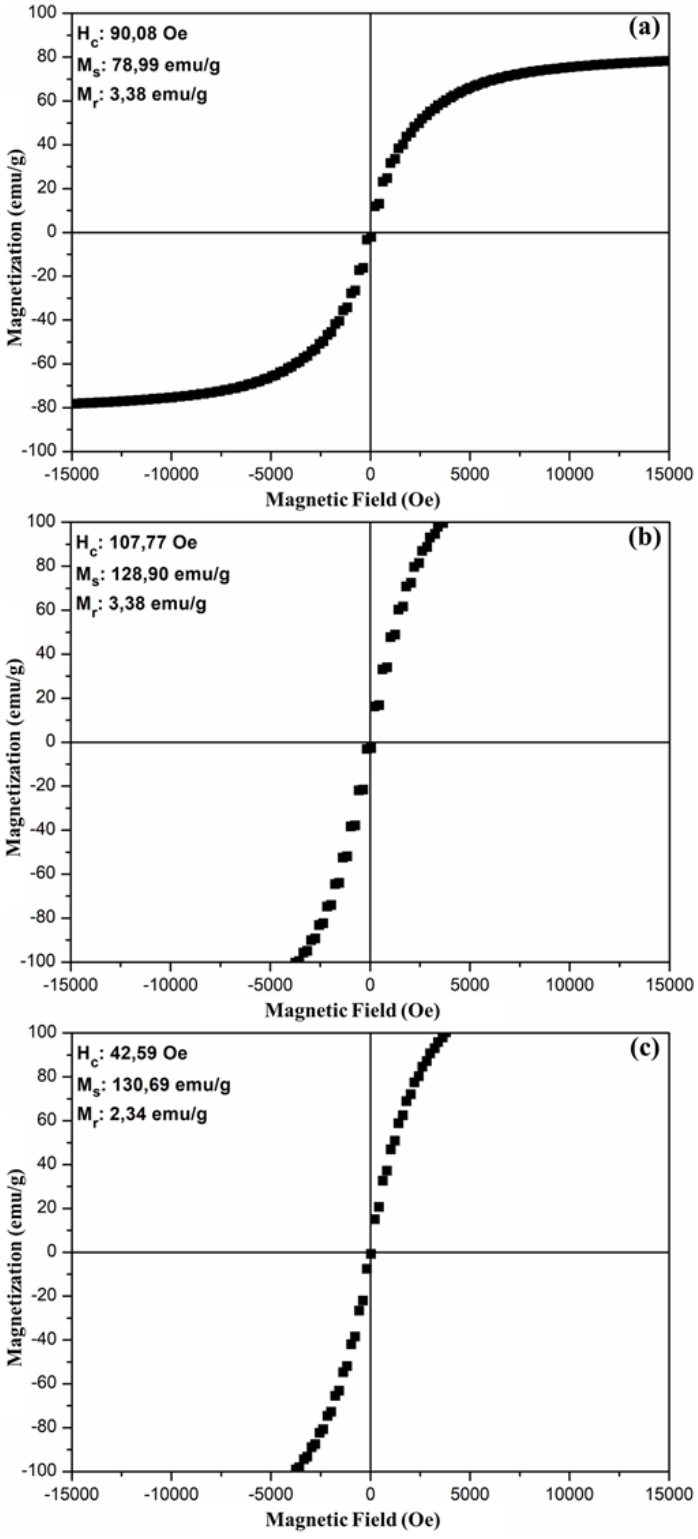

Figure 11. Hysteresis curves and VSM analysis results of the samples: **(a)** NFB1T, **(b)** NFB2T and **(c)** NFB3T.

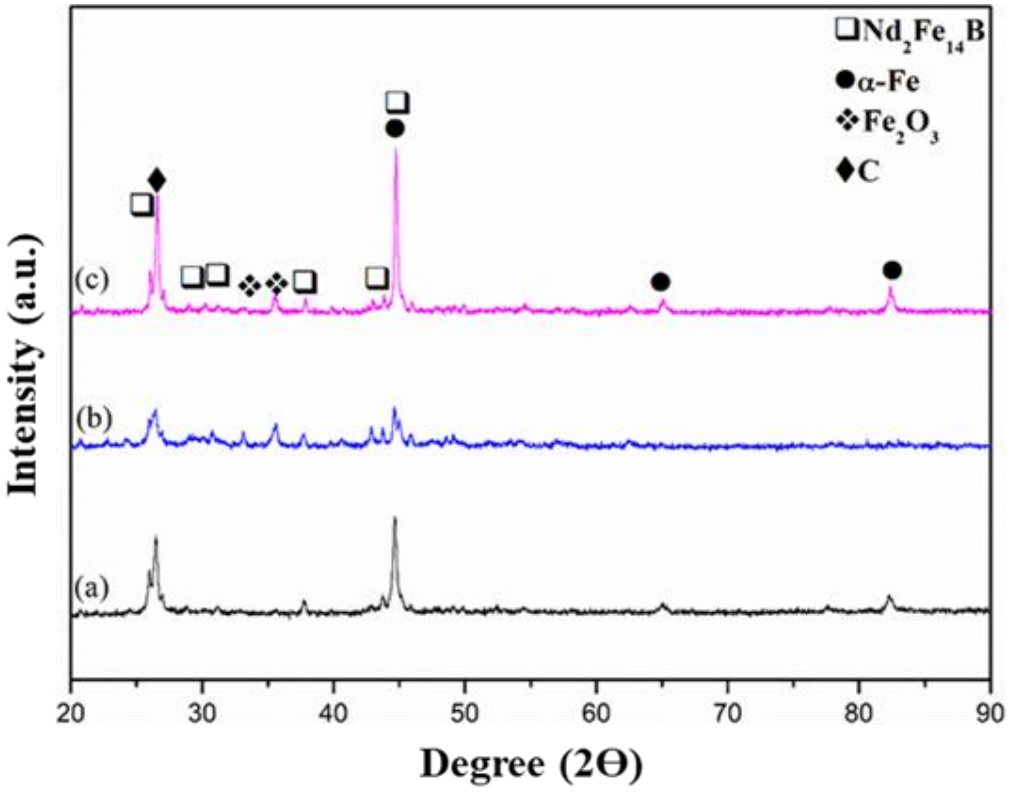

Figure 12. X-ray diffractometry results of the encapsulated samples produced from elemental raw materials: **(a)** NFB1TG, **(b)** NFB2TG and **(c)** NFB3TG.

Figure 13 presents SEM images of NFB1TG, NFB2TG and NFB3TG at 500×, 1000× and 1500× magnifications. The agglomerated spherical morphology observed in the annealed samples (Figure 9) is retained after CVD, indicating that 950°C treatment did not significantly alter particle arrangement or promote further sintering. The graphitic carbon shell is not resolvable at these magnifications; confirmation of the core-shell architecture relies on TEM analysis (Figure 16). The absence of observable morphological changes is consistent with a thin, conformal carbon coating that does not substantially modify particle dimensions, as expected for a thin, conformal graphitic carbon shell.

Figure 14 presents SEM elemental mapping of NFB1TG, NFB2TG and NFB3TG. In NFB1TG and NFB3TG, Nd, Fe, B and C show overlapping spatial distributions, indicating relatively uniform elemental co-distribution across agglomerate surfaces. In NFB2TG, Nd and Fe co-distribute as expected for the $Nd_2Fe_{14}B$ phase, while C and B signals are concentrated in coincident regions, suggesting locally non-uniform carbon distribution at the mapping scale. The spatial correlation of the carbon signal with the Nd-Fe-B nanoparticle regions supports successful CVD deposition, consistent with XRD findings. Oxygen is present in all samples, confirming persistence of the Fe_2O_3 surface oxide after encapsulation. Boron mapping should be considered semi-quantitative only (Goldstein et al., 2018).

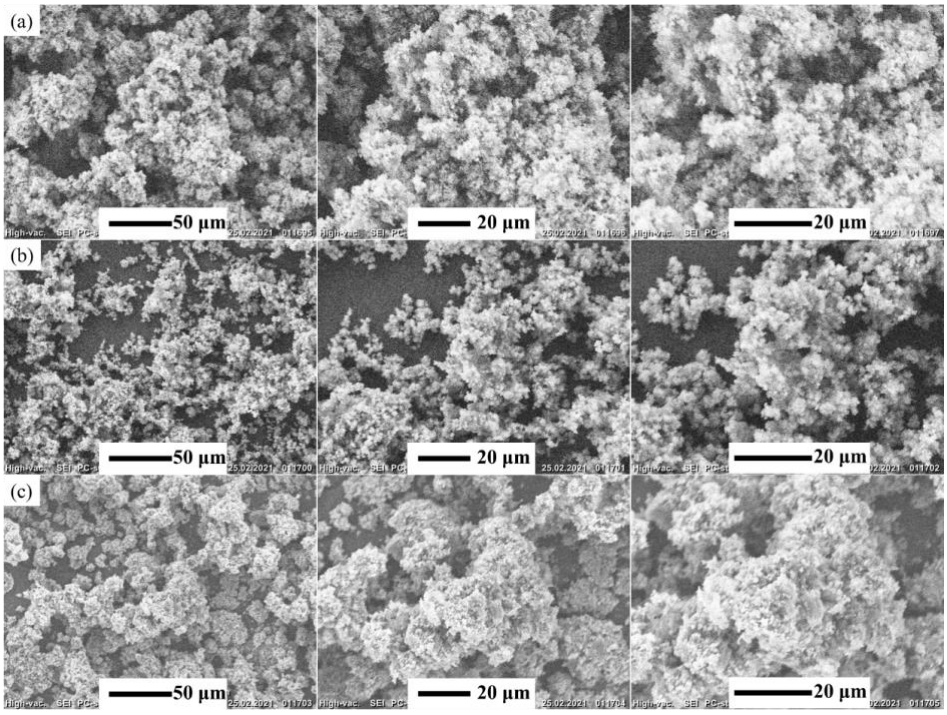

Figure 13. SEM images of the graphitic carbon shell encapsulated samples at 500X, 1000X and 1500X magnifications: **(a)** NFB1TG, **(b)** NFB2TG and **(c)** NFB3TG.

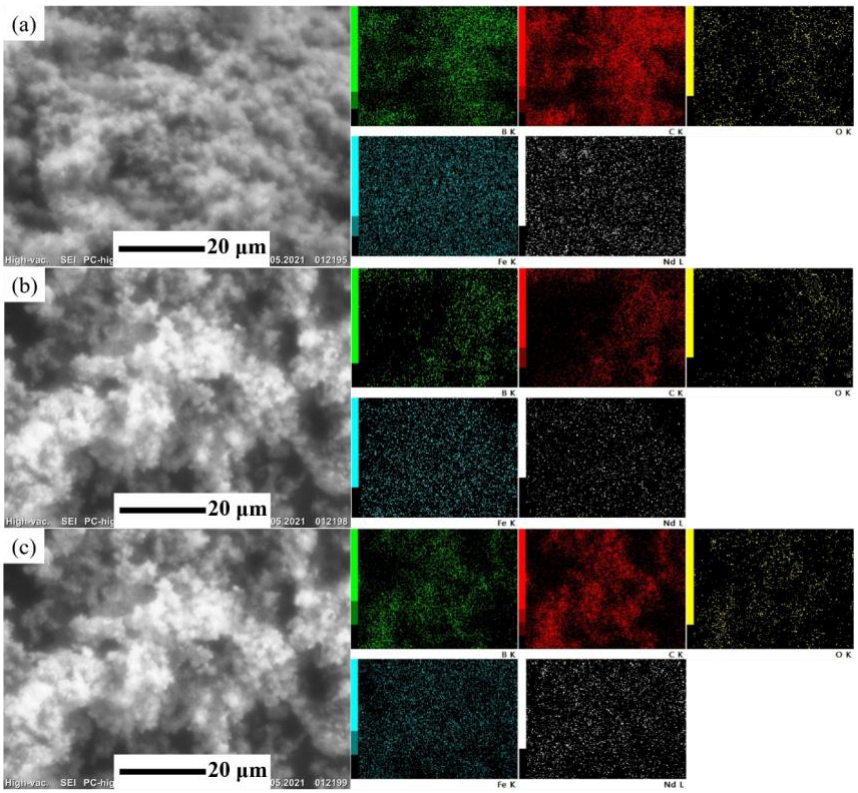

Figure 14. SEM images and elemental mapping analysis results of the encapsulated samples: **(a)** NFB1TG, **(b)** NFB2TG and **(c)** NFB3TG.

Figure 15 presents the VSM hysteresis curve of NFB2TG. Coercivity increased to 185.71 Oe from 107.77 Oe (NFB2T), attributed to the secondary annealing effect of CVD at 950°C, which promotes additional $Nd_2Fe_{14}B$ crystallization and enhances magnetocrystalline anisotropy (Popa et al., 2013). In contrast, saturation magnetization decreased substantially to 46.3 emu/g from 128.90 emu/g, a reduction of approximately 64%. Three contributing factors are proposed: the non-magnetic graphitic carbon shell adding sample mass without contributing to magnetization; further surface oxidation during CVD increasing Fe_2O_3 content; and possible partial surface disordering of the $Nd_2Fe_{14}B$ phase at elevated temperatures. The low Mr/Ms ratio of ~0.079 confirms an isotropic, exchange-decoupled nanoparticle system with significant non-magnetic phase content. Although 185.71 Oe represents the highest coercivity in this study, it remains well below values reported for bulk sintered Nd-Fe-B magnets (>10,000 Oe) and chemically synthesized $Nd_2Fe_{14}B$ nanoparticles (500-3000 Oe) (Rahimi et al., 2017). NFB2TG therefore exhibits semi-hard magnetic behavior, making it suitable for applications requiring moderate coercivity with enhanced chemical stability.

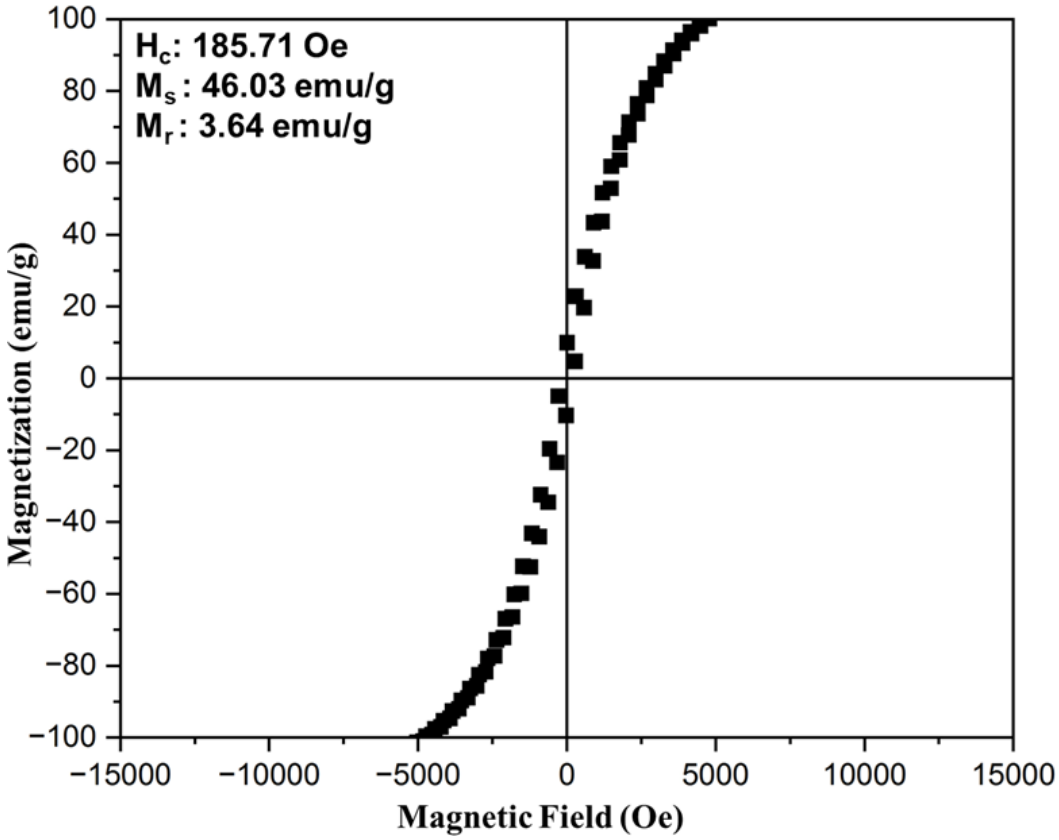

Figure 15. Hysteresis curve and VSM analysis results of the NFB2TG.

Figure 16 presents the TEM image of NFB2TG, confirming the core-shell architecture in which the Nd-Fe-B nanoparticle core is surrounded by a thin graphitic carbon shell. The carbon layers appear as continuous lattice fringes at the particle periphery, indicating a well-defined interfacial structure and successful carbon deposition. The regularity of these fringes suggests ordered graphitic stacking rather than amorphous carbon, though Raman spectroscopy or High-

resolution transmission electron microscopy (HRTEM) analysis would be required to conclusively determine the layer number and quality, an acknowledged limitation. The graphitic carbon shell is expected to act as a physical barrier against further oxidation of the Nd-Fe-B core and to improve thermal and chemical stability, supporting the suitability of this encapsulation approach for electronic applications.

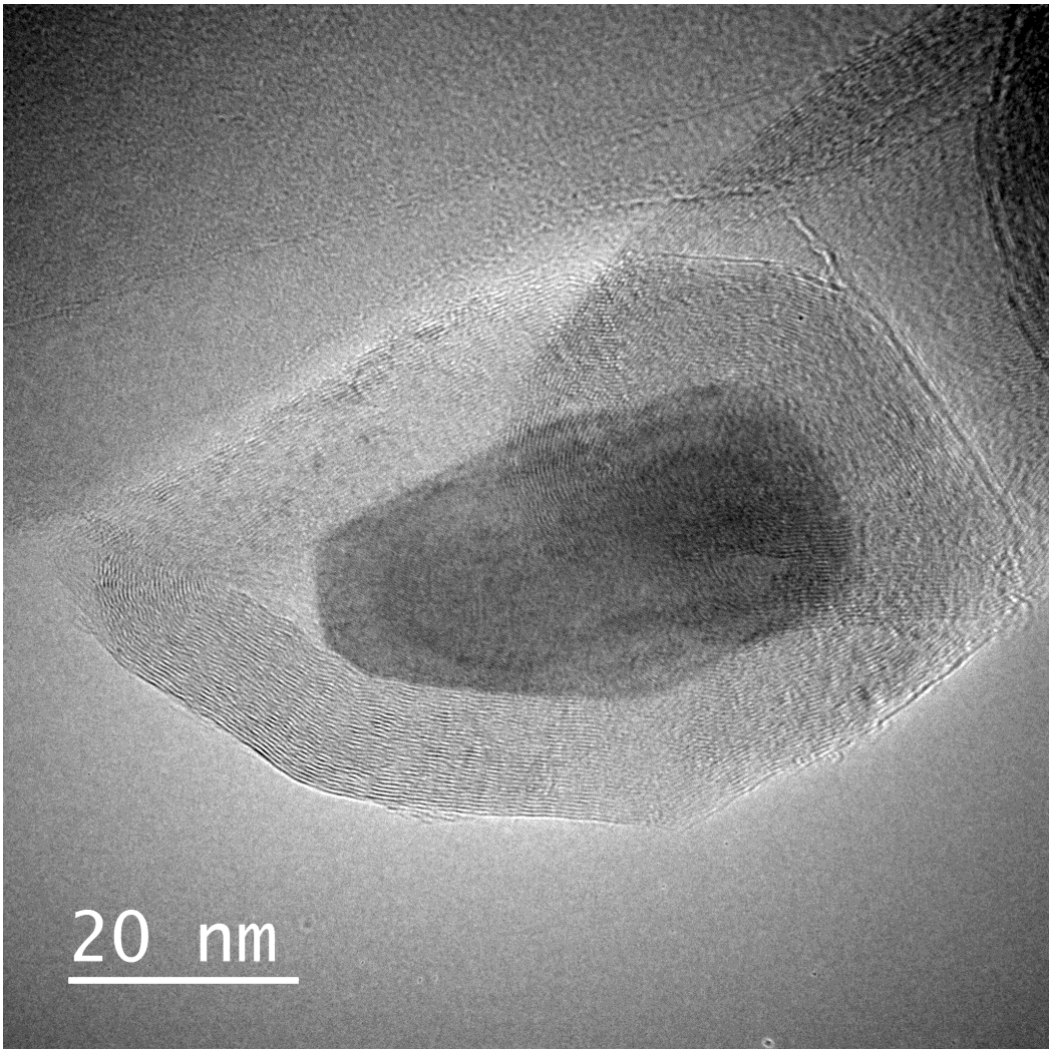

Figure 16. Transmission Electron Microscopy (TEM) image of the NFB2TG sample showing the core-shell nanostructure, with the Nd-Fe-B nanoparticle as the core surrounded by a thin graphitic carbon shell deposited via CVD.

4. Discussion

$Nd_{10}Fe_{84}B_6$ powders were synthesized by MA and subsequently annealed and graphitic carbon shell encapsulated. The apparent increase in DLS-measured particle size with longer milling durations reflects progressive agglomeration rather than true grain growth. Finer particles produced at extended milling times have higher surface areas and greater reactivity, making

them more susceptible to oxidation upon air exposure, which enhances interparticle attractive forces and promotes stronger agglomeration (Mehrifar et al., 2025).

Despite progressive coercivity improvements across the as-milled (54.81 Oe), annealed (107.77 Oe) and encapsulated (185.71 Oe) states, values remain well below those of bulk sintered Nd-Fe-B magnets (>10,000 Oe). This is attributed to three concurrent factors: the isotropic grain orientation inherent to MA-produced powders, which prevents texture-driven anisotropy development (Coey, 2010); the presence of non-magnetic Fe_2O_3 and soft magnetic α-Fe secondary phases, which create domain reversal nucleation sites and reduce the effective anisotropy field; and nanoparticle surface effects including disordered surface spins that suppress bulk magnetocrystalline anisotropy. The superior performance of the 10 h milled sample is attributed to an optimal balance between sufficient mechanical energy input for homogeneous phase distribution and the avoidance of excessive structural damage, agglomeration and oxidation associated with 12 h milling (Popa et al., 2013).

The substantial Ms decrease from 128.90 emu/g (NFB2T) to 46.3 emu/g (NFB2TG) following CVD encapsulation is attributed to the non-magnetic carbon shell contributing to sample mass without contributing to magnetization, further surface oxidation during processing at 950°C and possible partial surface disordering of the $Nd_2Fe_{14}B$ phase. Despite this reduction, the graphitic carbon shell provides a physical barrier against further oxidation and its secondary annealing effect improved crystallinity, reflected in the coercivity enhancement. This coercivity-Ms trade-off is a recognized challenge in carbon-encapsulated magnetic nanoparticle systems (Hosseinabadi et al., 2019).

The main limitations of this work are: (1) the absence of Raman spectroscopy and XPS and coating quality, so the carbon shell is referred to as a graphitic carbon shell throughout; (2) DLS reflects agglomerate hydrodynamic size rather than primary particle dimensions; (3) surface oxidation was not directly quantified by thermogravimetric or XPS analysis; and (4) only a single TEM image was presented, limiting statistical representativeness of the core-shell structure assessment.

5. Conclusion

Nd-Fe-B nanoparticles with the $Nd_{10}Fe_{84}B_6$ composition were successfully synthesized from elemental raw materials via mechanical alloying and subsequently annealed and encapsulated with a graphitic carbon shell via SCVD. Comprehensive characterization by XRD, DLS, SEM, EDS, VSM and TEM confirmed the formation of the $Nd_2Fe_{14}B$ tetragonal phase, with annealing at 900°C improving crystallinity and magnetic hardness. Among all samples, NFB2TG, produced by 10 h milling, annealing and encapsulation, exhibited the most favorable magnetic properties, with a coercivity of 185.71 Oe and a saturation magnetization of 46.3 emu/g. TEM confirmed a core-shell nanostructure with a continuous graphitic carbon layer surrounding the magnetic core. While coercivity values remain below those of bulk permanent magnets due to isotropic grain orientation, secondary phase content and nanoparticle surface effects inherent to the MA process, the combined approach of MA, annealing and CVD encapsulation

demonstrates a viable route for producing chemically stable Nd-Fe-B nanoparticles with semi-hard magnetic behavior, suitable for MEMS devices and magnetically recoverable systems.

Future work should focus on: (1) Raman spectroscopy and XPS to verify graphitic carbon shell quality and layer number; (2) TEM-based primary particle size analysis to distinguish primary particle dimensions from agglomerate sizes; (3) direct oxidation quantification by thermogravimetric analysis; (4) optimization of CVD parameters to minimize Ms loss during encapsulation; and (5) magnetic field-assisted annealing to introduce crystallographic texture and improve coercivity toward practical permanent magnet performance levels.

Conflict of Interest

The authors declare that they have no known competing financial interests or personal relationships that could have appeared to influence the work reported in this paper.

Funding

This research was supported by TENMAK National Boron Research Institute (BOREN) under the 2018 BK-1 Bor Scholarship Project and TÜBİTAK through the 1001 Project (Project Code: 118F430).

Acknowledgments

The authors would like to thank TENMAK National Boron Research Institute (BOREN) for supporting this thesis within the scope of the 2018 BK-1 Bor Scholarship Project. The authors also thank ASELSAN Electronics Industry Inc. for their support of this work within the framework of the TOHUM Project. Additionally, the budget of the TÜBİTAK 1001 project (Project Code: 118F430) was used to cover consumables and service costs for this thesis. The authors appreciate TÜBİTAK and their advisors for their contributions and guidance in deriving the thesis topic from this project. The authors also thank their colleagues Mustafa İlgen Kızılöz and Ayşegül Afal Geniş for their support during this work.

Ethical Statements

This study did not involve human or animal subjects. All experiments were conducted following institutional safety and laboratory regulations.

Data and Code Availability

All experimental data generated and analyzed during this study are available from the corresponding author upon reasonable request.

Supplementary Materials

Not applicable.

References

Ağaoğulları, D., Gökçe, H., Duman, İ., & Öveçoğlu, M. L. (2011). Characterization investigations of ZrB_2/ZrC ceramic powders synthesized by mechanical alloying of elemental Zr, B and C blends. *Journal of the European Ceramic Society*, *32*(7), 1447-1455. https://doi.org/10.1016/j.jeurceramsoc.2011.04.026

Ağaoğulları, D., Madsen, S. J., Öğüt, B., Koh, A. L., & Sinclair, R. (2017). Synthesis and characterization of graphite-encapsulated iron nanoparticles from ball milling-assisted low-pressure chemical vapor deposition. *Carbon*, *124*, 170-179. https://doi.org/10.1016/j.carbon.2017.08.043

Bystrzejewski, M., Lange, H., & Huczko, A. (2007). Carbon encapsulation of magnetic nanoparticles. *Fullerenes, Nanotubes and Carbon Nanostructures*, *15*(3), 167-180. https://doi.org/10.1080/15363830701236357

Chakka, V. M., Altuncevahir, B., Jin, Z. Q., Li, Y., & Liu, J. P. (2006). Magnetic nanoparticles produced by surfactant-assisted ball milling. *Journal of Applied Physics*, *99*(8), Article 08E912. https://doi.org/10.1063/1.2170593

Chen, W., Kim, J., Sun, S., & Chen, S. (2007). Composition effects of FePt alloy nanoparticles on the electro-oxidation of formic acid. *Langmuir*, *23*(22), 11303-11310. https://doi.org/10.1021/la7016648

Coey, J. M. D. (2010). *Magnetism and magnetic materials*. Cambridge University Press. https://doi.org/10.1017/CBO9780511845000

De Moraes, I. G., Fischbacher, J., Hong, Y., Naud, C., Okuno, H., Masseboeuf, A., Devillers, T., Schrefl, T., & Dempsey, N. M. (2024). Nanofabrication, characterisation and modelling of soft-in-hard FeCo-FePt magnetic nanocomposites. *Acta Materialia*, *274*, Article 119970. https://doi.org/10.1016/j.actamat.2024.119970

Dempsey, N. M. (2009). Hard magnetic materials for MEMS applications. In J. P. Liu, E. Fullerton, O. Gutfleisch, & D. J. Sellmyer (Eds.), *Nanoscale magnetic materials and applications* (pp. 661-683). Springer. https://doi.org/10.1007/978-0-387-85600-1_22

Goldstein, J. I., Newbury, D. E., Michael, J. R., Ritchie, N. W. M., Scott, J. H. J., & Joy, D. C. (2018). *Scanning electron microscopy and X-ray microanalysis* (4th ed.). Springer. https://doi.org/10.1007/978-1-4939-6676-9

Gubin, S. P., Spichkin, Y. I., Yurkov, G. Y., & Tishin, A. M. (2002). Nanomaterial for high-density magnetic data storage. *Russian Journal of Inorganic Chemistry*, *47*. https://amtc.ru/publications/articles/5rus.pdf

Hosseinabadi, S., Jafari, M. J., Kokabi, M., & Mohseni, M. (2019). Improving the electromagnetic shielding of fabricated Nd-Fe-B particles by a coating thin carbonaceous

layer. *Chemical Physics Letters*, *739*, Article 137015. https://doi.org/10.1016/j.cplett.2019.137015

Iacovacci, V., Lucarini, G., Innocenti, C., Comisso, N., Dario, P., Ricotti, L., & Menciassi, A. (2015). Polydimethylsiloxane films doped with Nd-Fe-B powder: Magnetic characterization and potential applications in biomedical engineering and microrobotics. *Biomedical Microdevices*, *17*(6), Article 112. https://doi.org/10.1007/s10544-015-0024-0

Jia, Z., Li, J., Gao, L., Yang, D., & Kanaev, A. (2023). Dynamic light scattering: A powerful tool for in situ nanoparticle sizing. *Colloids and Interfaces*, *7*(1), Article 15. https://doi.org/10.3390/colloids7010015

Jung, Y., Lee, Y., Yoon, S., & Choi, J. (2024). Synergistic effect of core/shell-structured composite fibers: Efficient recovery of rare-earth elements from spent Nd-Fe-B permanent magnets. *Advanced Fiber Materials*, *6*(6), 1729-1745. https://doi.org/10.1007/s42765-024-00442-4

Lee, S., Jeong, J., Shin, S., Kim, J., Chang, Y., Lee, K., & Kim, J. (2005). Magnetic enhancement of iron oxide nanoparticles encapsulated with poly(d,l-latide-co-glycolide). *Colloids and Surfaces A: Physicochemical and Engineering Aspects*, *255*(1-3), 19-25. https://doi.org/10.1016/j.colsurfa.2004.12.019

Lecerf, I., Angulo-Cervera, J. E., Orlandini-Keller, F., Moritz, P., Mathieu, F., Bourrier, D., Charlot, S., Nicu, L., Leïchlé, T., Devillers, T., Haettel, R., Dempsey, N. M., Blon, T., & Lacroix, L. (2025). A MEMS electromagnetic vibration energy harvester with monolithically integrated Nd-Fe-B micromagnets. *Advanced Materials Technologies*, *10*(10), Article 2401817. https://doi.org/10.1002/admt.202401817

Lim, J., Yeap, S. P., Che, H. X., & Low, S. C. (2013). Characterization of magnetic nanoparticle by dynamic light scattering. *Nanoscale Research Letters*, *8*, Article 381. https://doi.org/10.1186/1556-276X-8-381

Liu, Y. D., Choi, H. J., & Choi, S. (2012). Controllable fabrication of silica encapsulated soft magnetic microspheres with enhanced oxidation-resistance and their rheology under magnetic field. *Colloids and Surfaces A: Physicochemical and Engineering Aspects*, *403*, 133-138. https://doi.org/10.1016/j.colsurfa.2012.04.002

Manaf, A., Al-Khafaji, M., Zhang, P. Z., Davies, H. A., Buckley, R. A., & Rainforth, W. M. (1993). Microstructure analysis of nanocrystalline Fe-Nd-B ribbons with enhanced hard magnetic properties. *Journal of Magnetism and Magnetic Materials*, *128*(3), 307-312. https://doi.org/10.1016/0304-8853(93)90476-I

Mehrifar, Y., Moqtaderi, H., Hamidi, S. M., Golbabaei, F., Hasanzadeh, M., & Dehghan, S. F. (2025). Magnetic nanoparticles of $Nd_2Fe_{14}B$ prepared by ethanol-assisted wet ball milling technique. *Scientific Reports*, *15*(1), Article 3257. https://doi.org/10.1038/s41598-025-87301-3

Omelyanchik, A., Lamura, G., Peddis, D., & Canepa, F. (2020). Optimization of a Nd-Fe-B permanent magnet configuration for in-vivo drug delivery experiments. *Journal of Magnetism and Magnetic Materials*, *522*, Article 167491. https://doi.org/10.1016/j.jmmm.2020.167491

Ouyang, Y., Qiu, R., Xiao, Y., Shi, Z., Hu, S., Zhang, Y., Chen, M., & Wang, P. (2019). Magnetic fluid based on mussel inspired chemistry as corrosion-resistant coating of Nd-Fe-B magnetic material. *Chemical Engineering Journal*, *368*, 331-339. https://doi.org/10.1016/j.cej.2019.02.126

Périgo, E. A., Silva, S. C., De Sousa, E. M. B., Freitas, A. A., Cohen, R., Nagamine, L. C. C. M., Takiishi, H., & Landgraf, F. J. G. (2012). Properties of nanoparticles prepared from Nd-Fe-B-based compound for magnetic hyperthermia application. *Nanotechnology*, *23*(17), Article 175704. https://doi.org/10.1088/0957-4484/23/17/175704

Pich, A., Bhattacharya, S., Ghosh, A., & Adler, H. (2005). Composite magnetic particles: 2. Encapsulation of iron oxide by surfactant-free emulsion polymerization. *Polymer*, *46*(13), 4596-4603. https://doi.org/10.1016/j.polymer.2005.01.017

Popa, O., Dorolti, E., Borodi, G., Marcu, G., Coldea, M., & Turcu, R. (2013). The influence of milling and annealing on the structural and magnetic behavior of $Nd_2Fe_{14}B$/α-Fe magnetic nanocomposite. *Journal of Alloys and Compounds*, *574*, 496-501.

Rahimi, H., Ghasemi, A., Mozaffarinia, R., & Tavoosi, M. (2017). Magnetic properties and magnetization reversal mechanism of Nd-Fe-B nanoparticles synthesized by a sol-gel method. *Journal of Magnetism and Magnetic Materials*, *444*, 111-118. https://doi.org/10.1016/j.jmmm.2017.08.011

Saritas, E. U., Goodwill, P. W., Croft, L. R., Konkle, J. J., Lu, K., Zheng, B., & Conolly, S. M. (2012). Magnetic particle imaging (MPI) for NMR and MRI researchers. *Journal of Magnetic Resonance*, *229*, 116-126. https://doi.org/10.1016/j.jmr.2012.11.029

Savchenko, A. G., Menushenkov, V. P., Plastinin, A. Y., Zhukov, A. A., & Kuznetsov, P. A. (2018). Phase composition and magnetic properties of $Nd_2Fe_{14}B$/α-Fe nanocomposites prepared by mechanical alloying. *Russian Metallurgy (Metally)*, *2018*(4), 354-358. https://doi.org/10.1134/S0036029518040134

Schultz, L., Wecker, J., & Hellstern, E. (1987). Formation and properties of Nd-Fe-B prepared by mechanical alloying and solid-state reaction. *Journal of Applied Physics*, *61*(8), 3583-3585. https://doi.org/10.1063/1.338708

Sepehri-Amin, H., Ohkubo, T., Gruber, M., Schrefl, T., & Hono, K. (2014). Micromagnetic simulations on the grain size dependence of coercivity in anisotropic Nd-Fe-B sintered magnets. *Scripta Materialia*, *89*, 29-32. https://doi.org/10.1016/j.scriptamat.2014.06.020

Shen, L., Fan, M., Zhao, K., Qiu, M., & Tian, Z. (2018). Preparation and properties of nanocomposite coatings on sintered Nd-Fe-B magnets. *Materials Research Express*, *5*(8), Article 086401. https://doi.org/10.1088/2053-1591/aad121

Suryanarayana, C. (2010). Synthesis of nanocomposites by mechanical alloying. *Journal of Alloys and Compounds*, *509*(Suppl. 1), S229-S234. https://doi.org/10.1016/j.jallcom.2010.09.063

Tung, D. K., Manh, D. H., Phong, P. T., Phong, L. T. H., Dai, N. V., Nam, D. N. H., & Phuc, N. X. (2015). Structural and magnetic properties of mechanically alloyed $Fe_{50}Co_{50}$ nanoparticles. *Journal of Alloys and Compounds*, *640*, 34-38. https://doi.org/10.1016/j.jallcom.2015.04.022

Wu, K., Yao, Y., & Klik, I. (1997). Electrical and magnetic properties of Nd-Fe-B films. *Applied Surface Science*, *113-114*, 174-177. https://doi.org/10.1016/s0169-4332(96)00843-4

Yang, C., Ren, B., Wang, D., & Tang, Q. (2019). Synthesis of Nano-Fe@Nd-Fe-B/AC magnetic catalytic particle electrodes and application in the degradation of 2,4,6-trichlorophenol by electro-assisted peroxydisulfate process. *Environmental Technology*, *41*(19), 2464-2477. https://doi.org/10.1080/09593330.2019.1567826

Yang, H., Duan, L., Zhang, P., Xu, G., Cui, J., Lv, J., Sun, W., Li, B., Wang, D., & Wu, Y. (2022). Corrosion resistance of functionalized carbon nanotubes enhanced epoxy coatings on sintered Nd-Fe-B magnets. *Journal of Coatings Technology and Research*, *19*(5), 1317-1329. https://doi.org/10.1007/s11998-022-00641-x

Zhang, J., Wu, W., Meng, F., Ding, H., & Dong, J. (2018). Sol-gel-based chemical synthesis of Nd-Fe-B hard magnetic nanoparticles. *Modern Physics Letters B*, *32*(34n36), Article 1840070. https://doi.org/10.1142/s0217984918400705

Zhou, X., Tian, Y., Yu, H., Zhang, H., Zhong, X., & Liu, Z. (2019). Synthesis of hard magnetic Nd-Fe-B composite particles by recycling the waste using microwave assisted auto-combustion and reduction method. *Waste Management*, *87*, 645-651. https://doi.org/10.1016/j.wasman.2019.02.050